

Magnetic Resonance Simulation of Effective Transverse Relaxation (T_2^*)

Hidenori Takeshima  ^a

^a*MRI Systems Development Department, MRI Systems Division,
Canon Medical Systems Corporation, Kanagawa, Japan*

Abstract

Purpose: To simulate effective transverse relaxation (T_2^*) as a part of MR simulation. T_2^* consists of reversible (T_2') and irreversible (T_2) components. Whereas simulations of T_2 are easy, T_2' is not easily simulated if only magnetizations of individual isochromats are simulated.

Theory and Methods: Efficient methods for simulating T_2' were proposed. To approximate the Lorentzian function of T_2' realistically, conventional simulators require 100+ isochromats. This approximation can be avoided by utilizing a linear phase model for simulating an entire Lorentzian function directly. To represent the linear phase model, the partial derivatives of the magnetizations with respect to the frequency axis were also simulated. To accelerate the simulations with these partial derivatives, the proposed methods introduced two techniques: analytic solutions, and combined transitions.

For understanding the fundamental mechanism of the proposed method, a simple one-isochromat simulation was performed. For evaluating realistic cases, several pulse sequences were simulated using two phantoms with and without T_2' simulations.

Results: The one-isochromat simulation demonstrated that T_2' simulations were possible. In the realistic cases, T_2' was recovered as expected without using 100+ isochromats for each point. The computational times with T_2' simulations were only 2.0 to 2.7 times longer than those without T_2' simulations. When the above-mentioned two techniques were utilized, the analytic solutions accelerated 19 times, and the combined transitions accelerated up to 17 times.

Conclusion: Both theory and results showed that the proposed methods simulated T_2' efficiently by utilizing a linear model with a Lorentzian function, analytic solutions, and combined transitions.

Keywords: MR simulation, Bloch equations, T_2^* , T_2'

1. Introduction

Acquisition processes of an MR system can be simulated with the Bloch equations and their extensions[1, 2, 3]. Software for simulating these processes is often referred to as MR simulators. The simulators are useful for developing, prototyping, and evaluating various components of MR systems such as pulse sequences, image reconstruction, and postprocessing. Pulse sequences are simulated by updating time-dependent magnetizations of isochromats, and integrating these magnetizations whenever data sampling is requested. The output samples are integrals of these magnetizations in spatial and frequency axes.

There are two representations of isochromats: discrete and continuous representations. The simulators using the discrete representations[4, 5, 6, 7, 8, 9, 10, 11, 12, 13, 14, 15] assigned discrete points in continuous space to individual isochromats. In these simulators, the integrals were implemented as summations. In contrast, the simulators using the continuous representation[16] assigned small regions in continuous space to individual isochromats. All points in each region were treated as continuous. The magnetizations of these continuous points were represented as a constant magnitude with a linear phase model.

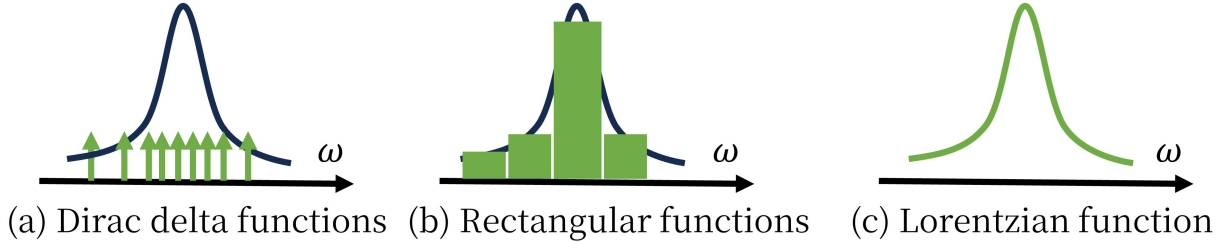


Figure 1: Various T_2' models. (a) A set of the Dirac delta functions. (b) A set of the rectangular functions. (c) A Lorentzian function. Whereas the models (a) and (b) approximates a Lorentzian function to be simulated with a set of functions, the model (c) uses the Lorentzian function to be simulated directly.

The purpose of this paper is to develop a precise and efficient simulation method of the effective transverse relaxation (T_2^*). T_2^* consists of irreversible (T_2) and reversible (T_2') components. Whereas it is easy to simulate T_2 , there were no known ways to simulate T_2' efficiently. Since many simulators used the discrete representations, a common way for simulating T_2' was to add a Lorentzian noise to magnetic field inhomogeneity[7, 9, 14]. When the simulated number of discrete isochromats was increased, its behaviors approached asymptotically to the true behaviors. However, as explained later, realistic T_2' simulations require 100+ isochromats for each point. In practice, the number of isochromats cannot be increased sufficiently since computational costs are roughly proportional to the number of isochromats. Even without increasing the number, many MR simulators needed to reduce computational costs and thus relied on hardware acceleration such as multi-threading [7, 10, 14, 15], single instruction multiple data (SIMD) [10, 14, 15], general-purpose graphics processing unit (GPGPU) [8, 9, 10, 13], computer clusters [6, 7], and cloud computing [11].

In this paper, efficient methods for simulating T_2' using a continuous representation were proposed. To simulate T_2' efficiently, a theory for simulating T_2' with only one isochromat was derived. For understanding the fundamental mechanism of the proposed method, this theory was experimentally confirmed by comparing the difference between discrete and continuous representations using a simple case. Realistic T_2^* simulations were also demonstrated using a house-made MR simulator.

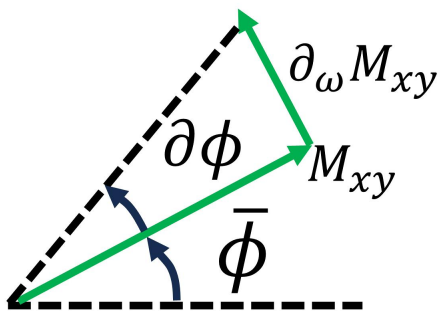
2. Theory

2.1. Baseline Methods

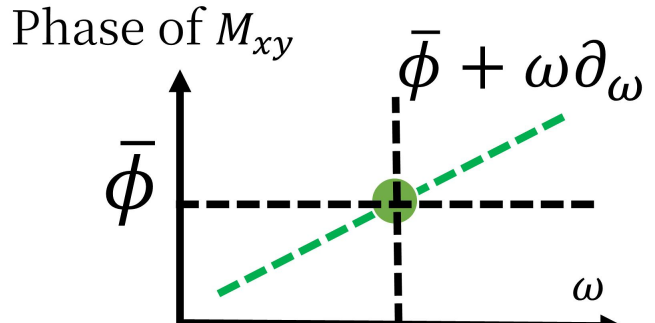
Let the direction of the static magnetic field be the z axis. Let the remaining axes representing the rotating frame around the z axis be the x and y axes. For the k -th isochromat ($k = 1, \dots, K$), the Bloch equations [1] were defined as

$$\frac{d\mathbf{M}_3(k, t)}{dt} = \gamma(\mathbf{M}_3(k, t) \times \mathbf{B}(k, t)) + \text{diag}(1/T_2(k), 1/T_2(k), 1/T_1(k))((0, 0, 1)^T - \mathbf{M}_3(k, t)) \quad (1)$$

where γ , $\mathbf{M}_3(k, t) = (M_x(k, t), M_y(k, t), M_z(k, t))^T$, $\mathbf{B}(k, t) = (B_x(k, t), B_y(k, t), B_z(k, t))^T$, $T_1(k)$, and $T_2(k)$ represent the gyromagnetic ratio, the *normalized* time-dependent magnetization vector at the time t , the magnetic field vector at the time t , longitudinal relaxation time, and transverse relaxation time, respectively. The relaxation times are given as a part of a phantom. The time-dependent magnetization vector $\mathbf{M}_3(k, t)$ is updated in a simulation process.



(a) M_{xy} and $\partial_\omega M_{xy}$



(b) Linear phase model

Figure 2: A continuous representation. (a) Relationship between a transverse magnetization and its partial derivative with respect to ω . The transverse magnetization is orthogonal to its partial derivative. (b) A linear phase model. The transverse magnetization M_{xy} is modeled as a constant magnitude with a phase linearly changed in the ω axis.

The magnetic field vector $\mathbf{B}(k, t)$ consists of $\mathbf{B}_1(k, t)$ and $\mathbf{B}_z(k, t)$. $\mathbf{B}_1(k, t) = B_x(k, t) + iB_y(k, t)$ represents the radiofrequency (RF) pulses. $\mathbf{B}_z(k, t)$ consists of several components and is represented as

$$\gamma B_z(k, t) = \gamma G(\mathbf{r}(k, t), t) + \gamma \Delta B_0(\mathbf{r}(k, t)) + d(k) + \omega \quad (2)$$

where $\mathbf{r}(k, t) = (r_x(k, t), r_y(k, t), r_z(k, t))^T$ represents the location of the isochromat, $G(\mathbf{r}(k, t), t)$ represents the magnetic fields from the gradient coils, $\Delta B_0(\mathbf{r}(k, t))$ represents the magnetic field inhomogeneity, $d(k)$ represents the chemical shift, and ω represents the perturbation come from the reversible transverse relaxation. In the cases of static isochromats, the time t of $\mathbf{r}(k, t)$ can be omitted. In the cases of linear gradient coils with no gradient imperfections, $G(\mathbf{r}(k, t), t)$ is defined as

$$G(\mathbf{r}(k, t), t) = G_x(t)r_x(k, t) + G_y(t)r_y(k, t) + G_z(t)r_z(k, t) \quad (3)$$

where $G_x(t)$, $G_y(t)$, and $G_z(t)$ represent gradients of a pulse sequence along x , y , and z axes, respectively.

When RF pulses $\mathbf{B}_1(k, t)$ are not used (referred to as without-RF subsequences), the magnetization at t can be computed analytically as

$$\mathbf{M}_{xy}(k, t) = \mathbf{M}_{xy}(k, t_0) \exp\left(-\frac{t - t_0}{T_2(k)}\right) \exp\left(\int_{t_0}^t -i\gamma B_z(k, t) dt\right), \text{ and} \quad (4)$$

$$M_z(k, t) = 1 + (M_z(k, t_0) - 1) \exp\left(-\frac{t - t_0}{T_1(k)}\right) \quad (5)$$

where $\mathbf{M}_{xy}(k, t)$ is defined as $\mathbf{M}_{xy}(k, t) = M_x(k, t) + iM_y(k, t)$.

When RF pulses $\mathbf{B}_1(k, t)$ are used (referred to as with-RF subsequences), iterative update is required for computing the time-dependent magnetization vector. If the magnetic field vector $\mathbf{B}(k, t)$ is piecewise constant between t and $t + \Delta t$, the transition of the time-dependent magnetization vector between t and $t + \Delta t$ can be represented as matrix multiplications by introducing the 4-dimensional vector $\mathbf{M}_4(k, t) = (M_x(k, t), M_y(k, t), M_z(k, t), 1)^T$. For a small duration Δt , the transition from t to $t + \Delta t$ can be written as

$$\mathbf{M}_4(k, t + \Delta t) = \mathbf{D}_4(k, \Delta t) \mathbf{R}_4(k, t, t + \Delta t) \mathbf{M}_4(k, t) \quad (6)$$

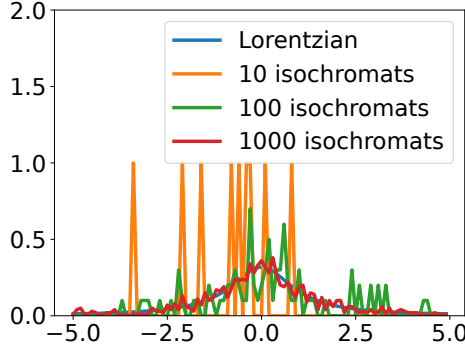


Figure 3: An example case of approximating a Lorentzian function using a set of thin rectangular functions. The function approximated with 10 isochromats is far from the Lorentzian function. There are still spike-like errors in the function approximated with 100 isochromats. The function approximated with 1000 isochromats is similar to the Lorentzian function. These functions show that at least 100+ rectangular functions are required for better approximation.

where $\mathbf{D}_4(k, \Delta t)$ and $\mathbf{R}_4(k, t, t + \Delta t)$ are 4×4 matrices given in Appendix A.

The computation of Eq. (6) can be accelerated by computing combined transitions once and using the combined transitions multiple times[4, 5, 12, 14] since many pulse sequences use same RF pulses repeatedly. By combining $\mathbf{D}_4(k, \Delta t)\mathbf{R}_4(k, t, t + \Delta t)$ at $t = t_0, t_1, \dots, t_{N_{RF}-1}$, a combined transition from t_0 to $t_{N_{RF}}$ can be represented as

$$\mathbf{M}_4(k, t_{N_{RF}}) = \mathbf{C}_4(k, t_0, t_{N_{RF}})\mathbf{M}_4(k, t_0) \quad (7)$$

where

$$\mathbf{C}_4(k, t_0, t_{N_{RF}}) = \mathbf{D}_4(k, \Delta t)\mathbf{R}_4(k, t_{N_{RF}-1}, t_{N_{RF}}) \cdots \mathbf{D}_4(k, \Delta t)\mathbf{R}_4(k, t_0, t_1) \quad (8)$$

represents the combined transition from t_0 to $t_{N_{RF}}$.

When a pulse sequence indicates use of analog-to-digital converters (ADCs), integrals of transverse magnetizations at specified times are computed. For the l -th receiver coil, the integral $A(l, t)$ can be represented as

$$A(l, t) = \sum_{k=1}^K \int_{-\infty}^{\infty} \int_{-\infty}^{\infty} \int_{-\infty}^{\infty} \int_{-\infty}^{\infty} w_l(\mathbf{r}(k, t), t) M_0(k) \mathbf{M}_{xy}(k, t) f_x(x - r_x) f_y(y - r_y) f_z(z - r_z) f_{\omega}(\omega) d\omega dz dy dx. \quad (9)$$

where $w_l(\mathbf{r}(k, t), t)$ represents the receiver coil sensitivity at the location $\mathbf{r}(k, t)$, $M_0(k)$ represents the scaling factor of the k -th isochromat, and $f_p(p)$ represents the magnitude and phase function relative to the rectangular center along the $p \in x, y, z, \omega$ axis. In the discrete representations shown in Fig. 1(a), $f_p(p)$ are the Dirac delta functions for all axes. In these cases, Eq. (9) is simplified as

$$A(l, t) = \sum_{k=1}^K w_l(\mathbf{r}(k, t), t) M_0(k) \mathbf{M}_{xy}(k, t). \quad (10)$$

To use continuous representations, Jochimsen et al.[16] used a linear-phase model for representing $f_p(p)$ as a parametric function (Fig. 2). For a region covered by an isochromat, its magnitudes are modeled as constant. The phases ϕ_p are modeled as $\phi_p(p) = \bar{\phi}_p + p \partial_p \phi_p$ where $\bar{\phi}_p$ represents the phase at the center,

and ∂_p represents a partial derivative with respect to p . The linear coefficient $\partial_p \phi_p$ can be computed as

$$\partial_p \phi_p = \frac{M_x(k, t) \partial_p M_y(k, t) - M_y(k, t) \partial_p M_x(k, t)}{\sqrt{M_x(k, t)^2 + M_y(k, t)^2}}. \quad (11)$$

To compute the linear coefficient, it is necessary to simulate $\partial_p \mathbf{M}_3(k, t)$ for computing $\partial_p \phi_p$. Jochimsen et al.[16] simulated $\partial_p \mathbf{M}_3(k, t)$ by approximating $\mathbf{B}_1(k, t)$ as piecewise constants for individual isochromats, and computing approximated partial derivatives of the transition Eq. (6). The partial derivatives of the transition from t to $t + \Delta t$ can be written as

$$\partial_p \mathbf{M}_3(k, t + \Delta t) = \mathbf{D}_3(k, \Delta t) \mathbf{R}_{3,xy}(k, t, t + \Delta t) \{ \partial_p \mathbf{R}_{3,z}(k, t, t + \Delta t) \mathbf{M}_3(k, t) + \mathbf{R}_{3,z}(k, t, t + \Delta t) \partial_p \mathbf{M}_3(k, t) \}. \quad (12)$$

The approximation process and matrices used in Eq. (12) are given in Appendix A. In Eq. (12), the last element of $\partial_p \mathbf{M}_4(k, t)$ is omitted since it is 0 for all p 's.

Jochimsen et al. treated isochromats as rectangular functions in both spatial and frequency axes. In their model, $f_p(p)$ is defined as $(1/L) \exp(i\phi_p(p))$ if $|p| < L/2$ and 0 otherwise (Fig. 1(b)).

2.2. Continuous Representation for Simulating T'_2

Conventional MR simulators sampled ω from the Lorentzian whose half-width at half-minimum was $1/T'_2$. In these simulators, 100+ isochromats per a discrete point are required in the ω axis for simulating T'_2 realistically as shown in Fig. 3. Use of the continuous representation with rectangular functions cannot solve this problem.

Rather than using a set of points or rectangular functions for representing T'_2 , $f_\omega(\omega)$ is modeled as

$$f_\omega(\omega) = \ell(\omega; 0, 1/T'_2(k)) \exp(i\omega \partial\phi_\omega(\omega)) \quad (13)$$

where $\ell(\omega; 0, 1/T'_2(k))$ represents a Lorentzian function whose mode and scale parameter are 0 and $1/T'_2(k)$, respectively (Fig. 1(c)). The remaining functions $g_x(x)$, $g_y(y)$, and $g_z(z)$ are the Dirac delta function.

By computing the integration parts of Eq. (9) with Fourier transforms, the integration value $A(l, t)$ becomes

$$A(l, t) = \sum_{k=1}^K w_l(\mathbf{r}(k, t), t) M_0(k) \mathbf{M}_{xy}(k, t) \exp\left(-\left(1/T'_2(k)\right) |\partial\phi_\omega(\omega)|\right). \quad (14)$$

Pseudo-code for simulation with Eq. (14) is given in Supplementary Material S1.

2.3. Analytic Solutions of Without-RF Subsequences for Computing Partial Derivatives

In the cases of without-RF subsequences, the partial derivatives of Eqs. (4) and (5) can be computed analytically for accelerating simulations. The partial derivative of Eq. (4) with respect to p can be computed as

$$\partial_p \mathbf{M}_{xy}(k, t) = \exp\left(-\frac{t-t_0}{T_2(k)}\right) \left((\partial_p \mathbf{M}_{xy}(k, t_0)) \exp\left(\int_{t_0}^t -i\gamma B_z(k, t) dt\right) + \mathbf{M}_{xy}(k, t_0) \left\{ \partial_p \exp\left(\int_{t_0}^t -i\gamma B_z(k, t) dt\right) \right\} \right). \quad (15)$$

In the case of $p = \omega$, Eq. (15) can be simplified as

$$\partial_\omega \mathbf{M}_{xy}(k, t) = \exp\left(-\frac{t-t_0}{T_2(k)}\right) \left((\partial_\omega \mathbf{M}_{xy}(k, t_0)) \exp\left(\int_{t_0}^t -i\gamma B_z(k, t) dt\right) - i(t-t_0) \mathbf{M}_{xy}(k, t_0) \exp\left(\int_{t_0}^t -i\gamma B_z(k, t) dt\right) \right). \quad (16)$$

since $\partial_\omega \int_{t_0}^t \gamma B_z(k, t) dt$ is $(t - t_0)$ according to Eq. (2).

The partial derivative of Eq. (5) with respect to p can be computed as

$$\partial_p \mathbf{M}_z(k, t) = \partial_p \mathbf{M}_z(k, t_0) \exp\left(-\frac{t-t_0}{T_1(k)}\right). \quad (17)$$

Pseudo-code for simulation with Eq. (16) and Eq. (17) is given in Supplementary Material S1.

2.4. Combined Transitions for Computing Partial Derivatives

In the cases of with-RF subsequences, it is useful to compute combined transitions and apply them repeatedly for accelerating simulations. To rewrite Eqs. (6) and (12) for systematic matrix operations, non-zero elements of both $\mathbf{M}_4(k, t)$ and $\partial_p \mathbf{M}_3(k, t)$ are merged as a 7-dimensional vector

$$\mathbf{M}_7(k, t) = (M_x(k, t), M_y(k, t), M_z(k, t), 1, \partial_p M_x(k, t), \partial_p M_y(k, t), \partial_p M_z(k, t))^T. \quad (18)$$

By using this vector, Eq. (12) can be represented as

$$\mathbf{M}_7(k, t + \Delta t) = \mathbf{D}_7(k, \Delta t) \mathbf{R}_7(k, t, t + \Delta t) \mathbf{M}_7(k, t). \quad (19)$$

The 7×7 matrices introduced in Eq. (19) are given in Appendix A. Since Eq. (19) is same as Eq. (6) except for the matrix sizes, the combined transition $\mathbf{C}_7(k, t_0, t_{N_{RF}})$ can be utilized for accelerating update of $\mathbf{M}_7(k, t)$ with existing reuse methodology[4, 5, 12, 14]. Similar to Eq. (8), $\mathbf{C}_7(k, t_0, t_{N_{RF}})$ can be represented as

$$\mathbf{C}_7(k, t_0, t_{N_{RF}}) = \mathbf{D}_7(k, \Delta t) \mathbf{R}_7(k, t_{N_{RF}-1}, t_{N_{RF}}) \cdots \mathbf{D}_7(k, \Delta t) \mathbf{R}_4(k, t_0, t_1). \quad (20)$$

Since the size of matrices are extended from 4×4 to 7×7 , straightforward computation of $\mathbf{C}_7(k, t_0, t_{N_{RF}})$ increases the computational times. To avoid 7×7 matrix multiplications in computing $\mathbf{C}_7(k, t_0, t_{N_{RF}})$, simulations of 7 linearly independent vectors of $\mathbf{M}_7(k, t)$ with Eqs. (6) and (19) can be used instead. An example set of these vectors is 7 unit vectors whose fourth elements are set to 1.

Pseudo-code for efficient computation of $\mathbf{C}_7(k, t_0, t_{N_{RF}})$ is given in Supplementary Material S1.

3. Methods

3.1. A Simple Case for Understanding the Fundamental Mechanism

A simple case was implemented and simulated for better understanding of the proposed method. In this case, there is only one isochromat whose physical values were $M_0 = 1$, $T_1 = 1/10$, $T_2 = 1/50$, and $T'_2 = 1/200$ ($T_2^* = 1/250$ since $1/T_2^* = 1/T_2 + 1/T'_2$). The pulse sequence to be simulated was a 15-millisecond Carr-Purcell-Meiboom-Gill (CPMG) sequence with no gradients. This sequence consisted of the first with-RF subsequence, the first without-RF subsequence, the second with-RF subsequence, and the second without-RF subsequence. The first and second with-RF subsequences contained 2-millisecond sinc RF pulses whose flip angles were adjusted to 90 and 180 degrees, respectively. The phase of the second with-RF subsequence was set to 90 degrees. The durations of the first and second without-RF subsequences were 3 and 8 milliseconds, respectively. There were no RF pulses in these without-RF subsequences.

In this simulation, all with-RF subsequences were simulated with Eqs. (6) and (19). All without-RF subsequences were simulated with Eqs. (4), (5), (16) and (17). Temporal dynamics of B_x , B_y , M_x , M_y , M_z , $\partial_\omega M_x$, $\partial_\omega M_y$, $\partial_\omega M_z$, and measured transverse magnetizations to be sampled were plotted. The measured transverse magnetizations were computed for both simulations with and without T'_2 .

3.2. Phantoms with Multiple Isochromats

Two phantoms named circles- T_2^* and brain- T_2^* were created for evaluating the proposed method in realistic conditions. The numbers of isochromats were 20 and 284 million for circles- T_2^* and brain- T_2^* , respectively.

The circles- T_2^* phantom was a numeric phantom which consisted of a large cylinder and 9 concentric cylinders which contained two cylinders with different diameters. These concentric cylinders were put in the large cylinder. All M_0 values in the large cylinder were shared. In each concentric cylinder, T_1 and T_2

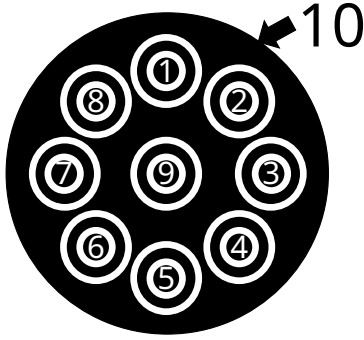


Figure 4: The layout of the circles- T_2^* phantom. There were a large cylinder and 9 pairs of concentric cylinders. The T_1 , T_2 , and T_2' values of all cylinders are given in Table 1.

Table 1: The T_1 , T_2 , and T_2' values of the cylinders used in the circles- T_2^* phantom. All values are given in second. Its layout is given in Fig. 4.

Cylinder	T_1	T_2	T_2' (Outer)	T_2' (Inner)
#1	0.20	0.05	0.04	0.02
#2	0.40	0.05	0.04	0.02
#3	0.60	0.05	0.04	0.02
#4	0.80	0.05	0.04	0.02
#5	1.00	0.05	0.04	0.02
#6	1.00	0.10	0.08	0.04
#7	0.80	0.10	0.08	0.04
#8	0.60	0.10	0.08	0.04
#9	0.40	0.10	0.08	0.04
#10	2.00	0.05	0.08	0.04

values of its two cylinders were shared. T_2' values of its two cylinders were not shared. Therefore, each concentric cylinder should be visible as the single cylinder in the cases of spin-echo sequences, and as the concentric cylinders in the cases of gradient-echo sequences. All ΔB_0 values were set to 0 Hz. The matrix and spatial sizes of the phantom were $960 \times 960 \times 48$ and $240\text{mm} \times 240\text{mm} \times 12\text{mm}$, respectively. The spatial resolution of this phantom was $0.25\text{mm} \times 0.25\text{mm} \times 0.25\text{mm}$. The layout and parameters of this phantom are given in Fig. 4 and Table 1, respectively.

The brain- T_2^* phantom was generated from multi-slice images of a brain and an artificial T_2' map. The matrix and spatial sizes of the phantom were $256 \times 240 \times 48$ and $256\text{mm} \times 240\text{mm} \times 240\text{mm}$, respectively. The multi-slice images were acquired in a volunteer scan. These images were same as the images used in a previous paper[14]. The M_0 , T_1 , and T_2 maps were generated from these images using a parameter mapping method similar to the method. The details of the parameter mapping method were given in Supplementary Material S2. All ΔB_0 values were set to 0 Hz. The artificial T_2' map was created as the following two steps. First, the map was filled with T_2' of 1/5. Second, two dots whose sizes were $3 \times 3 \times 3$ pixels were overwritten with T_2' of 1/100. Therefore, signals of these dots were expected to be decayed quickly in the cases of gradient-echo sequences. In the simulation, each voxel was divided into $4 \times 4 \times 20$ subvoxels for adjusting spatial resolution of this phantom to $0.25\text{mm} \times 0.25\text{mm} \times 0.25\text{mm}$. The volunteer scan was approved by

Table 2: Pulse sequences used in realistic simulations. These pulse sequences were available as examples of the Pulseq[17]. Abbreviations: T1W, T1-weighted, T2W, T2-weighted, SE, spin echo, RARE, rapid acquisition with relaxation enhancement, EPI, echo planar imaging.

	SPGR	RARE	EPI	Spiral
Sequence name	gre.seq	tse.seq	epi.seq	spiral.seq
RF pulse type	sinc	sinc	sinc	Gaussian (fat sat), sinc (excite)
Num. samples in RF pulses (1 us/sample)	3000 (excite)	2500 (excite) 2000 (refocus)	3000 (excite)	8000 (fat sat) 3000 (excite)
Num. with-RF	128	153	3	8
Num. unique RF pulses	1	2	3	5
Num. repeated RF pulses	127	151	0	3
FOV (mm \times mm)	256×256	256×256	220×220	256×256
Slice thickness (mm)	3	5	3	3
TR (ms)	12	2000	N/A	N/A
Approx. TE (ms)	5	100	26	3
Num. readout samples	128	128	64	13000
Num. phase encodes	128	128, ETL=16 1 dummy shot	64	N/A
Num. slices	1	1	3	4
Readout sampling ratio (us/sample)	25	50	4	1.6
Reconstruction matrix	256×256	256×256	256×256	256×256
Oversampling factor in gridding	2.0	2.0	4.5	2.0

our institutional review board and informed consent was obtained from the volunteer.

3.3. Evaluations with Multiple Isochromats

The proposed method was implemented as a part of house-made software named a virtual MR scanner (VMRscan)[14]. In the simulations using the VMRscan, multi-threading and SIMD instructions were used on a central processing unit (CPU). When with-RF subsequences were simulated, the step size of the simulations was set to 1 microsecond for compatibility with the Pulseq[17]. The brain- T_2^* phantom was split into 8 partial phantoms for reducing memory footprint. The simulations with individual partial phantoms were processed sequentially, and the sampled data via simulated ADCs were merged for image reconstruction. The computational times using the brain- T_2^* phantom were calculated by summing measured computational times of all partial phantoms. The software was run on a central processing unit (CPU) with 8 performance cores, 16 efficient cores and 32 processor threads. The frequencies of the CPU were 3.2 GHz for the performance cores and 2.4 GHz for the efficient cores. These cores were dynamically boosted up to 6.0 GHz.

To evaluate the efficiency of the analytic solutions given as Eqs. (16) and (17), computational times of an FID sequence were measured using the proposed method. The FID sequence consisted of an with-RF subsequence and an without-RF subsequence. The with-RF subsequence contained a 500-microsecond sinc pulse with no gradients. The without-RF subsequence was a 9500-microsecond delay with no RF pulses and gradients. The efficiency was evaluated by running the proposed method with and without Eqs. (16) and (17). The former and latter cases are referred to as FID-analytic and FID-update. When these equations

Table 3: Processing times using the (a) circles- T_2^* and (b) brain- T_2^* phantoms, in second. The number of isochromats in the brain- T_2^* phantom was 14 times greater than that in the circles- T_2^* phantom. With no accelerations, the computational times with T_2' was 2.0 to 2.2 times longer than those without T_2' . The computational times of the FID-analytic was 19 times faster than those of the FID-update. With combined transitions, the computational times were up to up to 17 times faster if many RF pulses were repeated.

(a) Circles- T_2^* (20068128 isochromats)						
	FID-update	FID-analytic	SPGR	RARE	EPI	Spiral
No T_2'	18.36	0.97	750.11	614.53	34.52	153.92
T_2'	39.93	2.14	1609.19	1334.54	72.65	315.48
No T_2' + combined	34.26	2.00	45.51	52.65	50.67	143.20
T_2' + combined	86.99	5.16	93.37	111.27	117.16	321.44
(b) Brain- T_2^* (280152000 isochromats)						
	FID-update	FID-analytic	SPGR	RARE	EPI	Spiral
No T_2'	251.41	13.18	10159.93	8443.54	483.89	2077.85
T_2'	535.39	28.18	22020.83	17843.24	974.39	4415.70
No T_2' + combined	462.12	27.45	611.37	710.08	677.45	1924.95
T_2' + combined	1229.51	73.59	1323.49	1563.82	1654.42	4511.43

were not used, the without-RF subsequence was treated as a 9500-microsecond RF pulse whose shapes were all zeros. In either case, the with-RF subsequence was simulated with both Eqs. (19) and (20).

To evaluate the proposed method in realistic condition, acquisitions of four pulse sequences available as examples of the Pulseq[17] were simulated, and their images were reconstructed with a gridding algorithm. Their computational times were also measured with and without combined transitions. The sequence parameters of the pulse sequences are shown in Table 2. The following methods were evaluated.

No T_2' A conventional method without both T_2' and combined transitions.

No T_2' -combined A conventional method without T_2' and with combined transitions.

T_2' The proposed method without combined transitions.

T_2' -combined The proposed method with combined transitions.

In the cases of the conventional and proposed methods, the combined transitions were $C_4(k, t_0, t_{RF})$ and $C_7(k, t_0, t_{RF})$, respectively. In the case of the circles- T_2^* phantom, a conventional method whose ΔB_0 values were sampled from a Lorentzian function with T_2' (T_2' -random) was also used for simulating reconstruction images using a discrete representation.

4. Results

4.1. A Simple Case for Understanding the Fundamental Mechanism

The temporal dynamics of the simulation with the proposed method is shown in Fig. 5. Whereas M_y decayed monotonically with T_2 (Fig. 5(b)), $\partial_\omega M_x$ increased monotonically except the time around the refocusing pulse (Fig. 5(c)). Fig. 5(d) represent temporal dynamics of the measured transverse magnetization using an ADC with and without T_2' . Whereas measured transverse magnetization using Eq. (10) was same as M_x and M_y shown in Fig. 5(b), measured transverse magnetization using Eq. (14) included T_2' as expected.

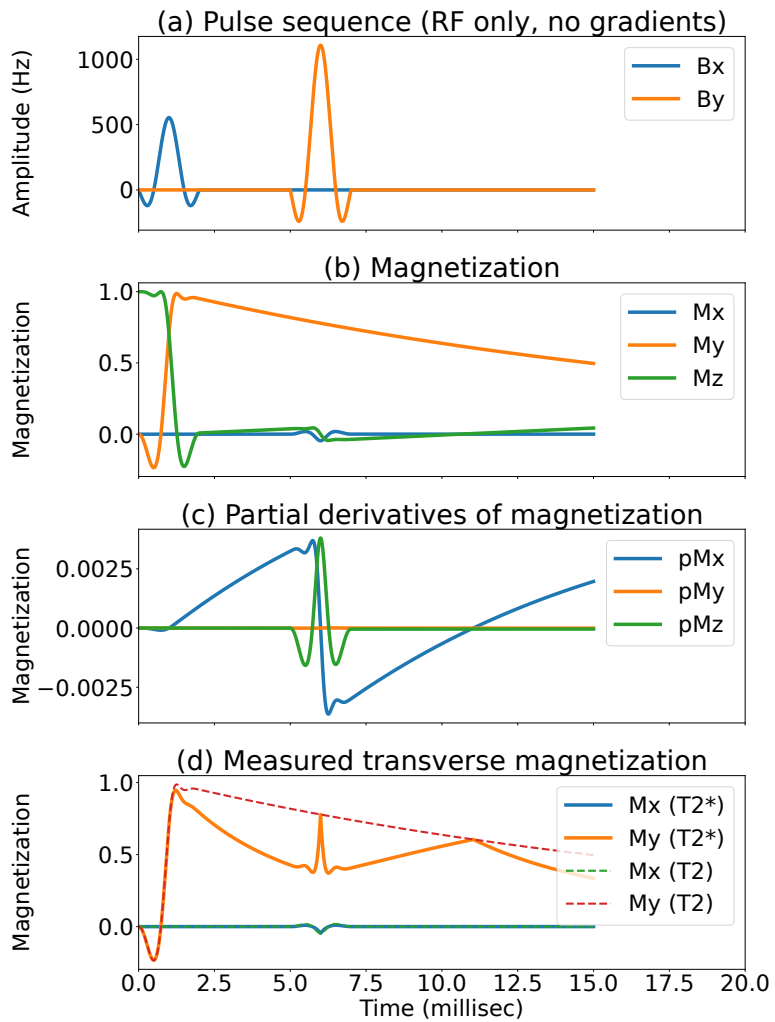


Figure 5: Temporal dynamics of (a) the simulated pulse sequence, (b) the magnetization vector, (c) its partial derivatives, and (d) measured transverse magnetization using an ADC with and without T_2' . As shown in (b), M_y decayed monotonically with T_2 . As shown in (c), $\partial_\omega M_x$ increased monotonically except the time around the refocusing pulse shown in (a). By simulating (b) only, T_2 decay was simulated. By simulating both (b) and (c), T_2^* decay could be simulated.

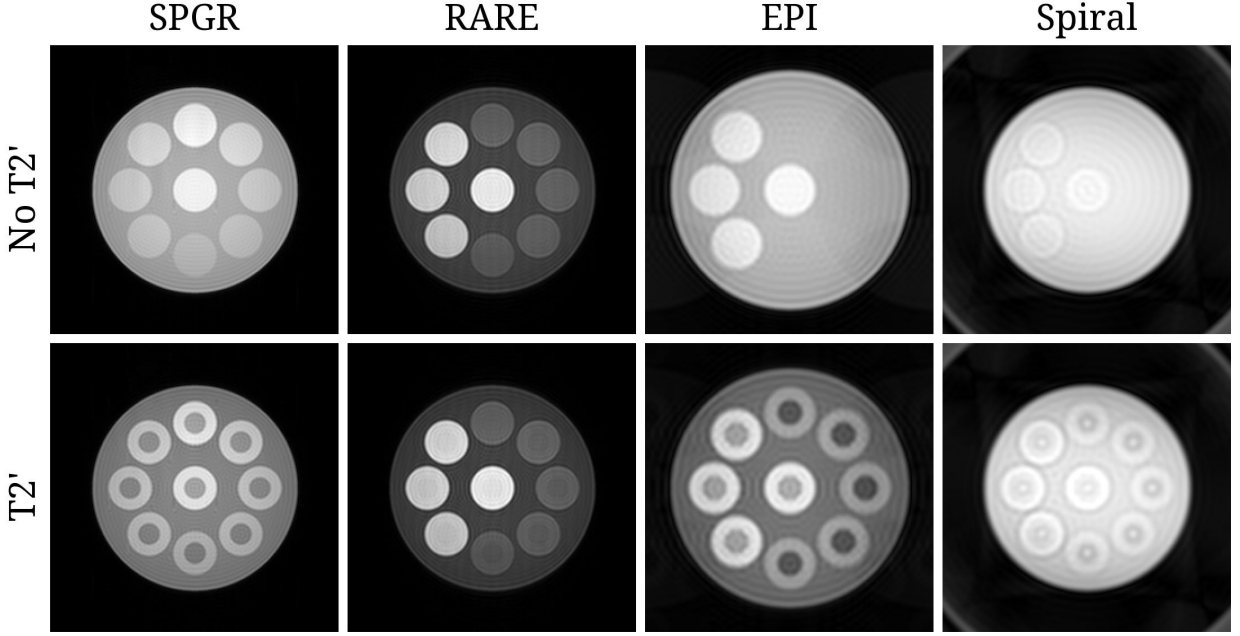


Figure 6: Reconstructed images using the circles- T_2^* phantom with four pulse sequences. Whereas the results without T_2' did not simulate inner concentric cylinders, the results with T_2' simulated inner concentric cylinders whose T_2^* values were different from outer concentric cylinders in the cases of gradient-echo sequences. It can also be confirmed that T_2 contrast images were reconstructed in the cases of the RARE sequence.

4.2. Evaluations with Multiple Isochromats

The computational times of both FID and Pulseq sequences are shown in Table 3. In all the evaluated cases, both number of isochromats and processing times of the brain- T_2^* phantom were approximate 14 times greater than those of the circles- T_2^* phantom. The computational times of the FID-analytic was 19 times faster than those of the FID-update. In the cases of the simulations with and without combined transitions, the computational times with T_2' was 2.0 to 2.2 times and 2.0 to 2.7 times longer than those without T_2' , respectively.

Reconstructed images using the circles- T_2^* phantom are shown in Fig. 6. Whereas the results without T_2' did not simulate inner concentric cylinders, the results with T_2' simulated inner concentric cylinders whose T_2^* values were different from outer concentric cylinders in the cases of gradient-echo sequences. It was also confirmed that only the outer concentric cylinders were reconstructed in the cases of the RARE sequence.

Reconstructed images using the brain- T_2^* phantom are shown in Fig. 7. In the cases of the circles- T_2^* phantom, As shown in the T_2' map, there were two dots whose T_2' values were low. By comparing the results with and without T_2' , two dots were reconstructed in the cases of gradient-echo sequences only if T_2' was simulated.

5. Discussion

The main contributions of this paper are to propose the novel simulation method of T_2' without relying on 100+ isochromats, and to demonstrate their efficiency of the proposed method experimentally. As derived in the Theory section, T_2' can be modeled by simulating $\mathbf{M}_7(k, t)$ instead of $\mathbf{M}_4(k, t)$ and using a linear phase model. Whereas the computational times for simulating T_2' were 2.0-2.7 times longer, the preciseness of the

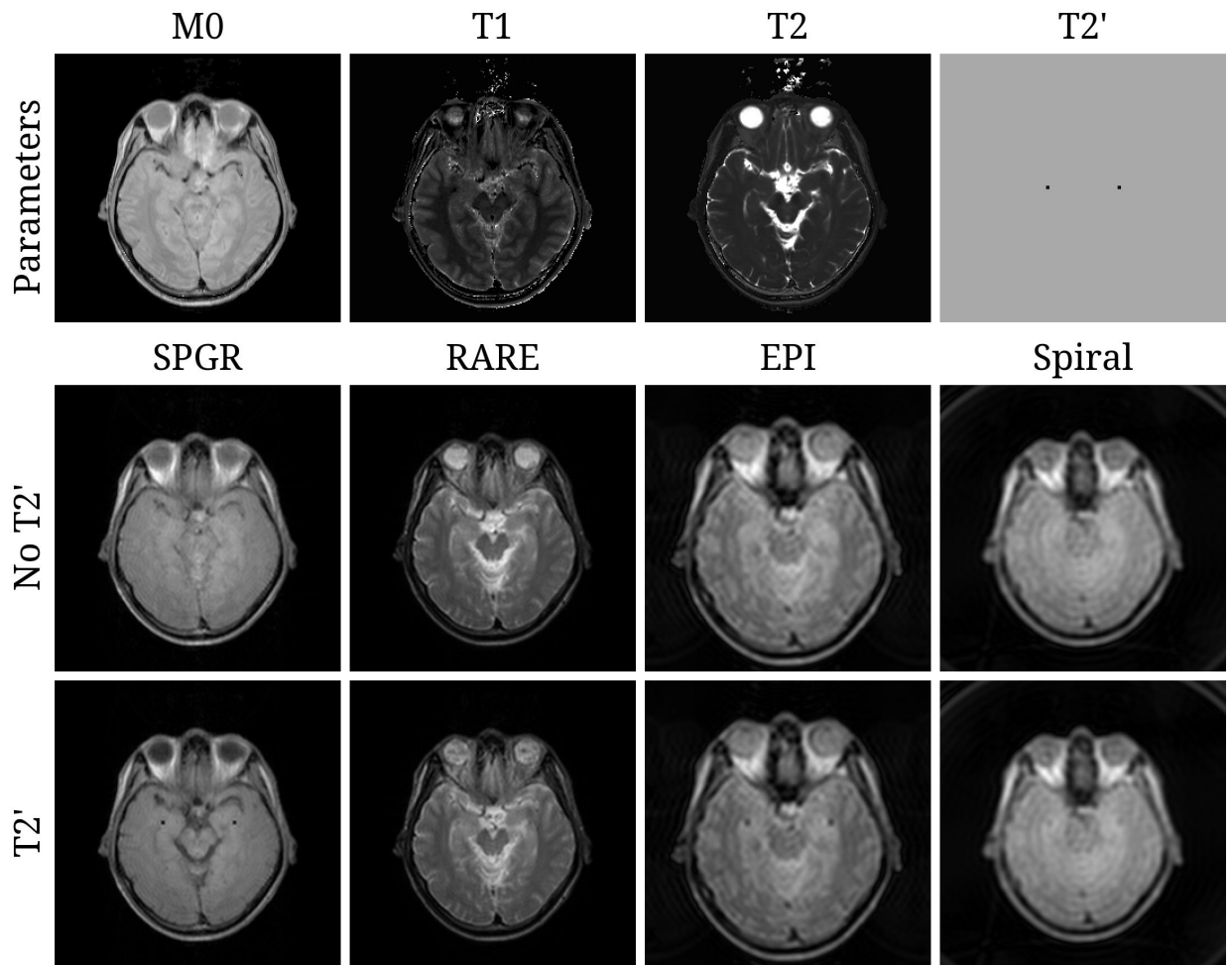


Figure 7: Reconstructed images using the brain- T_2^* phantom with four pulse sequences. As shown in the T_2' map, there were two dots whose T_2' values were low. By comparing the results with and without T_2' , two dots were reconstructed in the cases of gradient-echo sequences only if T_2' was simulated.

T'_2 decay was theoretically better than simulations of T'_2 with 100+ isochromats using conventional methods as shown in Fig. 1.

The simple case demonstrated that only one isochromat were required for T'_2 simulations if the partial derivatives of the magnetizations were available. Without this information, only T_2 decays could be simulated as shown in Fig. 5 (d). In addition, the temporal dynamics of the partial derivatives gave an insight into the relative strength of the T'_2 effects. It was not easy to get such information from the magnetizations only even if 100+ isochromats were used. Therefore, this simulation method is expected to be useful for understanding the principle of T_2 and T_2^* .

The evaluations with both the circles- T_2^* and brain- T_2^* phantoms showed that practical T'_2 simulations were possible without increasing the number of isochromats for modeling a Lorentzian function. The differences of the T_2^* values were easily confirmed as the visibilities of the inner concentric cylinders of the circles- T_2^* , and the dots of the brain- T_2^* phantoms. In addition, the computational times showed that the combined transitions[4, 5, 12, 14] were still efficient even when the size of the magnetization vectors were increased from 4 to 7. These results showed that combined transitions were useful in the cases of RF pulses which were reused at least 3 times. RF pulses which do not meet this criterion should be simulated directly with Eq. (19) whenever possible.

A fundamental limitation of the proposed method is utilization of the linear-phase model in entire Lorentzian functions. This model is incorrect if RF pulses used in a pulse sequence are highly frequency dependent. Future work includes simulations of such RF pulses more precisely.

6. Conclusion

Both theory and results showed that the proposed methods simulated T'_2 efficiently by utilizing a linear model with a Lorentzian function, analytic solutions, and combined transitions. Their fundamental mechanism was experimentally confirmed using a simple case, and their effectiveness was demonstrated using a house-made MR simulator with 284 million isochromats.

7. Disclosure Statement

Hidenori Takeshima is an employee of Canon Medical Systems Corporation.

Appendix A. Matrix Representations of Transitions and Their Partial Derivatives

According to the implementations used an asymmetric operator splitting method [18], the transition can be approximated as $\mathbf{D}_4(k, \Delta t)\mathbf{R}_4(k, t, t + \Delta t)$ where the matrices \mathbf{D}_4 and \mathbf{R}_4 represent relaxation and rotation, respectively. These matrices are given as

$$\mathbf{D}_4 = \begin{pmatrix} & & & 0 \\ & \mathbf{D}_3 & & 0 \\ & & & 1 - \exp(-\Delta t/T_1) \\ 0 & 0 & 0 & 1 \end{pmatrix}, \quad (\text{A.1})$$

$$\mathbf{D}_3 = \begin{pmatrix} \exp(-\Delta t/T_2) & 0 & 0 \\ 0 & \exp(-\Delta t/T_2) & 0 \\ 0 & 0 & \exp(-\Delta t/T_1) \end{pmatrix}, \quad (\text{A.2})$$

$$\mathbf{R}_4 = \begin{pmatrix} \mathbf{R}_3 & 0 \\ 0 & 0 \\ 0 & 0 & 1 \end{pmatrix}, \text{ and} \quad (\text{A.3})$$

$$\mathbf{R}_3 = \begin{pmatrix} \cos \theta + u_x u_x (1 - \cos \theta) & -u_z \sin \theta + u_x u_y (1 - \cos \theta) & u_y \sin \theta + u_x u_z (1 - \cos \theta) \\ u_z \sin \theta + u_x u_y (1 - \cos \theta) & \cos \theta + u_y u_y (1 - \cos \theta) & -u_x \sin \theta + u_y u_z (1 - \cos \theta) \\ -u_y \sin \theta + u_x u_z (1 - \cos \theta) & u_x \sin \theta + u_y u_z (1 - \cos \theta) & \cos \theta + u_z u_z (1 - \cos \theta) \end{pmatrix} \quad (\text{A.4})$$

where $(u_x, u_y, u_z) = \mathbf{B}(k, t)/|\mathbf{B}(k, t)|$ and $\theta = -\gamma|\mathbf{B}(k, t)|\Delta t$.

As used in Jochimsen et al.[16], the rotation matrix $\mathbf{R}_3(k, t, t + \Delta t)$ can be further approximated by processing rotations in the z direction separately as $\mathbf{R}_3(k, t, t + \Delta t) = \mathbf{R}_{3,xy}(k, t, t + \Delta t)\mathbf{R}_{3,z}(k, t, t + \Delta t)$. The matrix $\mathbf{R}_{3,xy}(k, t, t + \Delta t)$ corresponds to the matrix $\mathbf{R}_3(k, t)$ whose $B_z(k, t)$ of $\mathbf{B}(k, t)$ is replaced by zero. The matrix $\mathbf{R}_{3,z}(k, t, t + \Delta t)$ corresponds to the matrix $\mathbf{R}_3(k, t)$ whose $B_x(k, t)$ and $B_y(k, t)$ of $\mathbf{B}(k, t)$ are replaced by zeros. For the sake of convenience, $\mathbf{R}_{3,xy}(k, t, t + \Delta t)$ and $\mathbf{R}_{3,z}(k, t, t + \Delta t)$ are defined similarly. The matrix representations of these matrices are

$$\mathbf{R}_{3,xy} = \begin{pmatrix} \cos \theta_{xy} + u_x u_x (1 - \cos \theta_{xy}) & u_x u_y (1 - \cos \theta_{xy}) & u_y \sin \theta_{xy} \\ u_x u_y (1 - \cos \theta_{xy}) & \cos \theta_{xy} + u_y u_y (1 - \cos \theta_{xy}) & -u_x \sin \theta_{xy} \\ -u_y \sin \theta_{xy} & u_x \sin \theta_{xy} & \cos \theta_{xy} \end{pmatrix}, \text{ and} \quad (\text{A.5})$$

$$\mathbf{R}_{3,z} = \begin{pmatrix} \cos \theta_z & -\sin \theta_z & 0 \\ \sin \theta_z & \cos \theta_z & 0 \\ 0 & 0 & 1 \end{pmatrix} \quad (\text{A.6})$$

where θ_{xy} and θ_z represent θ calculated for $\mathbf{R}_{3,xy}(k, t, t + \Delta t)$ and $\mathbf{R}_{3,z}(k, t, t + \Delta t)$, respectively.

The partial derivative of the matrix $\mathbf{R}_{3,z}(k, t, t + \Delta t)$ with respect to p is

$$\partial p \mathbf{R}_{3,z} = \frac{\partial \theta_z}{\partial p} \begin{pmatrix} -\sin \theta_z & -\cos \theta_z & 0 \\ \cos \theta_z & -\sin \theta_z & 0 \\ 0 & 0 & 0 \end{pmatrix} \quad (\text{A.7})$$

where $\partial \theta_z / \partial p = -\Delta t$ in the case of $p = \omega$.

The 7×7 matrices $\mathbf{D}_7(k, \Delta t)$ and $\mathbf{R}_7(k, \Delta t)$, introduced in Eq. (19), are given as

$$\mathbf{D}_7 = \begin{pmatrix} \mathbf{D}_4 & \mathbf{0} \\ \mathbf{0} & \mathbf{D}_3 \end{pmatrix}, \text{ and} \quad (\text{A.8})$$

$$\mathbf{R}_7 = \begin{pmatrix} \mathbf{R}_4 & \mathbf{0} \\ \mathbf{R}_{3,xy} \partial_p \mathbf{R}_{3,z} & \mathbf{R}_{3,xy} \mathbf{R}_{3,z} \end{pmatrix}. \quad (\text{A.9})$$

References

- [1] F. Bloch, Nuclear induction, *Physical Review* 70 (1946) 460–474. doi:10.1103/PhysRev.70.460.
- [2] H. C. Torrey, Bloch equations with diffusion terms, *Physical Review* 104 (1956) 563–565. doi:10.1103/PhysRev.104.563.
- [3] H. M. McConnell, Reaction rates by nuclear magnetic resonance, *The Journal of Chemical Physics* 28 (3) (1958) 430–431. doi:10.1063/1.1744152.

[4] Y. Taniguchi, C. Nakaya, Y. Bito, E. Yamamoto, A high-speed MRI simulator using the transition matrix method and periodicity of magnetization (in Japanese), *IEICE Transaction on Information and Systems D-II* J77-D2 (1994) 566–572.

[5] Y. Taniguchi, C. Nakaya, Y. Bito, E. Yamamoto, A high-speed MRI simulator using the transition matrix method and periodicity of magnetization (translated from Japanese), *Systems and Computers in Japan* 26 (2) (1995) 54–62. doi:10.1002/scj.4690260206.

[6] H. Benoit-Cattin, G. Collewet, B. Belaroussi, H. Saint-Jalmes, C. Odet, The SIMRI project: a versatile and interactive MRI simulator, *Journal of Magnetic Resonance* 173 (1) (2005) 97–115. doi:10.1016/j.jmr.2004.09.027.

[7] T. Stöcker, K. Vahedipour, D. Pflugfelder, N. J. Shah, High-performance computing MRI simulations, *Magnetic Resonance in Medicine* 64 (1) (2010) 186–193. doi:10.1002/mrm.22406.

[8] C. G. Xanthis, I. E. Venetis, A. V. Chalkias, A. H. Aletras, MRISIMUL: A GPU-based parallel approach to MRI simulations, *IEEE Transactions on Medical Imaging* 33 (3) (2014) 607–617. doi:10.1109/TMI.2013.2292119.

[9] F. Liu, J. V. Velikina, W. F. Block, R. Kijowski, A. A. Samsonov, Fast realistic MRI simulations based on generalized multi-pool exchange tissue model, *IEEE Transactions on Medical Imaging* 36 (2) (2017) 527–537. doi:10.1109/TMI.2016.2620961.

[10] R. Kose, K. Kose, Blochsolver: A GPU-optimized fast 3D MRI simulator for experimentally compatible pulse sequences, *Journal of Magnetic Resonance* 281 (2017) 51–65. doi:10.1016/j.jmr.2017.05.007.

[11] C. G. Xanthis, A. H. Aletras, coreMRI: A high-performance, publicly available MR simulation platform on the cloud, *PLoS ONE* 14 (2019) e0216594. doi:10.1371/journal.pone.0216594.

[12] N. Scholand, C. Graf, M. Uecker, Efficient bloch simulation based on precomputed state-transition matrices, in: *Proceedings of the Joint Annual Meeting ISMRM-ESMRMB*, 2022, p. 748.

[13] C. Castillo-Passi, R. Coronado, G. Varela-Mattatall, C. Alberola-López, R. Botnar, P. Irarrazaval, Ko-maMRI.jl: An open-source framework for general MRI simulations with GPU acceleration, *Magnetic Resonance in Medicine* 90 (1) (2023) 329–342. doi:10.1002/mrm.29635.

[14] H. Takeshima, A fast and practical computation method for magnetic resonance simulators, *Magnetic Resonance in Medicine* 90 (2) (2023) 752–760. doi:10.1002/mrm.29646.

[15] H. Takeshima, Fast magnetic resonance simulation using combined update with grouped isochromats, *arXiv preprint* 2508.03960 (2025). doi:10.48550/arXiv.2508.03960.

[16] T. H. Jochimsen, A. Schäfer, R. Bammer, M. E. Moseley, Efficient simulation of magnetic resonance imaging with Bloch-Torrey equations using intra-voxel magnetization gradients, *Journal of Magnetic Resonance* 180 (1) (2006) 29–38. doi:10.1016/j.jmr.2006.01.001.

[17] K. J. Layton, S. Kroboth, F. Jia, S. Littin, H. Yu, J. Leupold, J.-F. Nielsen, T. Stöcker, M. Zaitsev, Pulseq: A rapid and hardware-independent pulse sequence prototyping framework, *Magnetic Resonance in Medicine* 77 (4) (2017) 1544–1552. doi:10.1002/mrm.26235.

[18] C. Graf, A. Rund, C. S. Aigner, R. Stollberger, Accuracy and performance analysis for bloch and bloch-mcconnell simulation methods, *Journal of Magnetic Resonance* 329 (2021) 107011. doi:10.1016/j.jmr.2021.107011.

Supplementary Materials

S1. Pseudo-code of the Key Components in the Proposed Method

The key components in the proposed method are simulations of T'_2 , fast simulations with analytic solutions, and fast simulations with combined transitions. For better understanding of the proposed method, this supplementary document provides pseudo-code for these key components.

The first key component is a sampling method for simulating T'_2 . This method includes simulations of Eqs. (14) and (19). Assuming that $\mathbf{M}_7(k, t)$'s are simulated at all t 's to be sampled via ADC. Simplified pseudo-code for sampling data can be written as follows. In the following pseudo-code, receiver coil sensitivity is omitted.

```

function M7_SAMPLING_T2STAR( $M_{7,t}, M_0, T'_2$ )
  for  $t$  in all times do
     $M7sampling \leftarrow M_{7,t}[t]$  ▷ M7 at the time t
     $M_x \leftarrow M7sampling[0]$  ▷ Extract elements of M7
     $M_y \leftarrow M7sampling[1]$ 
     $\partial M_x \leftarrow M7sampling[4]$ 
     $\partial M_y \leftarrow M7sampling[5]$ 
     $tmp \leftarrow \sqrt{M_x^2 + M_y^2}$  ▷ Compute a partial derivative of phi
     $tmp \leftarrow \max(tmp, 1^{-10})$  ▷ Avoid zero-division errors
     $\partial\phi \leftarrow (M_x * \partial M_y - M_y * \partial M_x) / tmp$  ▷ Compute a sample with T2-prime decay at t
     $sample \leftarrow M_0 * (M_x + 1j * M_y) * \exp(-(1/T'_2) * |\partial\phi|)$ 
     $allsamples[t] \leftarrow sample$ 
  end for
  return  $allsamples$ 
end function

```

The second key component is a fast simulation method using analytic solutions. The analytic solutions of the partial derivative elements of $\mathbf{M}_7(k, t)$ are derived as Eqs. (16) and (17). To compute remaining elements of $\mathbf{M}_7(k, t)$, Eqs. (4) and (5) are also required. Pseudo-code for updating with these analytic solutions can be written as follows.

```

function ANALYTIC_M7_UPDATE( $M_7$ , integral_Bz, duration,  $T_1, T_2$ )
   $M_{xy} \leftarrow M_7[0] + 1j * M_7[1]$  ▷ Extract elements of M7
   $M_z \leftarrow M_7[2]$ 
   $\partial M_{xy} \leftarrow M_7[4] + 1j * M_7[5]$ 
   $\partial M_z \leftarrow M_7[6]$ 
   $tmp \leftarrow \exp(-1j * integral_Bz)$  ▷ Precompute a rotation
   $\partial M_{xy} \leftarrow \exp(-duration/T_2) * (\partial M_{xy} * tmp - 1j * duration * M_{xy} * tmp)$  ▷ Compute partial derivatives of Mxy and Mz
   $\partial M_z \leftarrow \partial M_z * \exp(-duration/T_1)$ 
   $M_{xy} \leftarrow M_{xy} * \exp(-duration/T_2) * tmp$  ▷ Compute Mxy and Mz
   $M_z \leftarrow 1 + (M_z - 1) * \exp(-duration/T_1)$ 
  return [ $M_{xy}.real, M_{xy}.imag, M_z, 1, \partial M_{xy}.real, \partial M_{xy}.imag, \partial M_z$ ] ▷ Return updated M7
end function

```

The third key component is a fast simulation method using combined transitions. Straightforward computation of $\mathbf{C}_7(k, t_0, t_{N_{RF}})$ is possible but increases the computational times. To avoid 7×7 matrix multi-

plications in computing $C_7(k, t_0, t_{N_{RF}})$, simulations of 7 linearly independent vectors of $M_7(k, t)$ with Eq. (6) can be used instead. By using a set 7 unit vectors whose fourth elements are set to 1, pseudo-code for computing $C_7(k, t_0, t_{N_{RF}})$ without 7×7 matrix multiplications can be written as follows.

```

function MATRIX_C7_COMBINED( $B_x, B_y, B_z, \Delta t, T_1, T_2$ )
     $\triangleright$  Initial vectors. The fourth elements are constants and thus are set to 1.
    M7 = [
        [1,0,0,1,0,0,0],
        [0,1,0,1,0,0,0],
        [0,0,1,1,0,0,0],
        [0,0,0,1,0,0,0],
        [0,0,0,1,1,0,0],
        [0,0,0,1,0,1,0],
        [0,0,0,1,0,0,1]
    ]
    for  $t$  in all times do
        for  $v$  in 4, 5, 6 do  $\triangleright$  Update partial derivatives only on updating the last three vectors.
            M7[v][4:7]  $\leftarrow$  update_pM3(M7[v],  $B_x[t], B_y[t], B_z[t], \Delta t, T_1, T_2$ )
        end for
        for  $v$  in 0, 1, 2, 3 do  $\triangleright$  Update all elements.
            M7[v]  $\leftarrow$  update_M7(M7[v],  $B_x[t], B_y[t], B_z[t], \Delta t, T_1, T_2$ )
        end for
        for  $v$  in 4, 5, 6 do  $\triangleright$  Update M4 components of the last three vectors.
            M7[v][0:4]  $\leftarrow$  M7[3][0:4]
        end for
    end for
    for  $v$  in 0, 1, 2, 4, 5, 6 do  $\triangleright$  Since the fourth elements of the initial vectors are set to 1,
        M7[v]  $\leftarrow$  M7[v] - M7[3]  $\triangleright$  the following compensations are required.
    end for
    return transpose_matrix(M7)
end function

```

It is worth noting that update of $M_4(k, t)$ can be omitted on updating the last three vectors since $M_4(k, t)$ is independent from $\partial_\omega M_4(k, t)$.

S2. Parameter Mapping Method for Generating the Brain- T_2^* Phantom

Four T1-weighted (T1W) images, and four T2-weighted (T2W) images were acquired for generating parameter maps. All acquisitions shared the matrix and field-of-view (FOV) sizes. The following table describes pulse sequences used in the volunteer scan.

The T_1 and T_2 values were estimated using the following parameter mapping method. For each pixel, the best T_1 value was searched from 200 logarithmically-spaced candidate values. The candidate values were put in the range of 10 to 4500 milliseconds. Similarly, for each pixel, the best T_2 value was searched from 200 logarithmically-spaced candidate values. The candidate values were put in the range of 10 to 2500 milliseconds.

After the T_2 values were estimated, the M_0 values were estimated using all T2W images with a least-squares method. In the estimation of the M_0 values, the T_1 values were ignored. The pixels whose M_0

	T1W (4 acquisitions)	T2W
Sequence type	2D SE	2D RARE with 4 echos
Reconstruction matrix	$512 \times 480 \times 48$	$512 \times 480 \times 48$
FOV	$256 \times 240 \times 240 \text{ mm}^3$	$256 \times 240 \times 240 \text{ mm}^3$
Num. echos	1	4
TE	10 ms	20, 60, 100, 140 ms
TR	500, 800, 1100, 1500 ms	4500 ms

values were lower than a threshold were removed. To remove undesirable noises, pixels whose T_1 values were the maximum value (4500 milliseconds) were also removed.